Magnetic Field Enhancements in the Solar Wind: Diverse Processes Manifesting a Uniform Observation Type?

Ying-Dong Jia[1], Hairong Lai[2], Nathan Miles [1,3], Hanying Wei[1], Janet G. Luhmann[4], C. T. Russell[1], X. Blanco-Cano[5], Lan Jian[6], Chen Shi[1]

1 Department of Earth, Planetary, and Space Sciences, University of California, Los Angeles, CA, 90095, USA

2 Planetary Environmental and Astrobiological Research Laboratory (PEARL), School of Atmospheric Sciences, Sun Yat-sen University, Zhuhai, Guangdong, 519000, China

3 Cooperative Institute for Research in Environmental Sciences, CU Boulder, CO, 80309

4 Space Sciences Laboratory, University of California, Berkeley, CA, 94720, USA

5 Instituto de Geofisica, Universidad Nacional Autonoma de Mexico, CDMX, 04150, Mexico

6 Heliophysics Science Division, NASA Goddard Space Flight Center, Greenbelt, MD 20771, USA

Abstract

Within the solar wind throughout the inner heliosphere, observations reveal the presence of magnetic field enhancements accompanied by thin current sheets at varying distances from the sun and across different longitudes and latitudes. Two primary explanations have been proposed to elucidate these phenomena: Solar wind-dust interaction and interlacing flux ropes. In this study, we employ multi-fluid Magnetohydrodynamics (MHD) and Hall MHD models to simulate these hypotheses, respectively. Our findings indicate a concurrence between both models and the observed phenomena, suggesting that both processes may result in the same kind of enhancement. Furthermore, both models make predictions pointing to additional types of observational data, occurring at distinct spatial or temporal stages of the interaction. This convergence of model predictions with empirical data underscores the need for further observational and modeling studies to comprehensively test these models. This research enhances our knowledge of the inner heliosphere's dynamics and the influence of the solar wind on the Earth's magnetosphere, thereby shedding light on critical aspects of space weather and its potential impact on our planet.

Plain language abstract

In the vast region around the sun without any noticeable obstacles, scientists have noticed that sometimes the magnetic field gets stronger. There have been two main ideas proposed to explain why this happens: One is that ions and electrons from the sun interact with clouds of tiny dust particles, and the other proposes that two rope-like magnetic structures collide. To investigate these two quite different explanations, we have used two different computer models to simulate the process. We find that both models reproduce what we observe. In addition, these models also predict other signatures we should be able to see during these events. These predictions suggest that either mechanism may cause the enhancement phenomenon we observe, and more investigation is needed. Such research helps us understand how the particles in the vast space around the sun and its planets operate and how these processes may affect our planet.

Key points:

- Two different simulation models are presented, each based on a hypothesis that aims to explain the same type of solar wind phenomenon.
- Both models successfully reproduce the observed phenomena qualitatively, calling for additional research.
- Our models predict distinctive additional observation patterns, offering further ways of investigation.

1. Introduction

The solar wind is critical in shaping processes throughout the solar system, with its impact on Earth's magnetosphere being of particular significance to us. A century of extensive research has uncovered a wide range of structures in the solar wind, spanning large, meso, and kinetic scales (see Figure 1, Viall et al., 2021). Among these, mesoscale structures like small-scale magnetic flux ropes (MFRs) (e.g. Hu et al., 2018) and quasi-periodic proton density structures (PDSs) (Kepko et al., 2002) are also extensively studied, recognizing the complexity of solar wind.

In addition, there exists a distinct class of mesoscale structures that is characterized by a gradual amplification of interplanetary magnetic field (IMF) magnitude *B*, ranging from 20% to

200%, before symmetrically returning to the background value. This behavior has been observed after various spacecraft missions, including ACE, Wind, and STEREO. The initial observation was made by Russell et al. (1983), who termed these phenomena "Interplanetary Field Enhancements" (IFEs).

Previously established properties of IFEs include:

(1) Scale: At 1 AU, IFEs last from minutes to hours in in-situ spacecraft data (Arghavani et al., 1985). They are smaller than large-scale structures like interplanetary coronal mass ejections (ICMEs) and stream interaction regions (SIRs), but larger than the near-kinetic-scale mirror mode waves (e.g. Russell et al., 2008) and interplanetary discontinuities (e.g. Burlarga, 1971; Liu et al., 2022).

(2) Field and Plasma Conditions: At the peak magnitude of an IFE, the orientation of the magnetic field often undergoes abrupt changes, yet the variations in plasma parameters usually remain below 10% (Lai et al., 2013). This discrepancy between field and plasma pressures leaves the energy source driving the field enhancement in IFEs yet unidentified.

(3) Propagation Speed: The first reported IFE was observed by the Pioneer Venus Orbiter, later followed by Venera 13 and 14 near Venus, albeit further from the Sun. With multi-spacecraft conjunction observations, the time delays suggest that these structures move at the speed of the solar wind (Russell et al., 1985; Lai et al., 2015).

(4) Interface Normal: Initially, the observed gradual intensification of IMF B and its sudden rotation of vector $\mathbf{B}$ components at the central current sheet were thought to resemble interactions similar to those of comets in the solar wind (Russell et al., 1986). However, unlike a comet's tail which aligns closely with the solar wind, the magnetic field reversals deduced in IFEs do not exhibit a uniform pattern regarding the angle between the normal direction of the interface and the solar wind (e.g., Fragette et al., 2021). This indicates that the direction of interaction flow is not solely governed by the solar wind.

(5) Occurrence Rate: The annual detection rate of IFEs at 1 AU is about 8/year (Arghavani et al., 1985; Lai et al., 2013). This rate remains constant regardless of heliocentric distance until it begins to decrease beyond 2AU. In contrast, the rate increases at higher heliocentric ecliptic (HE) latitudes. Additionally, these occurrences tend to cluster temporally and longitudinally (Lai et al., 2014). Further statistical analysis has indicated that IFEs predominantly cluster in regions downstream of the orbits of asteroids or comets (Russell et al., 1984; Johns et al., 2003; Connors

et al., 2016).

Russell et al. (1984) postulated that IFEs result from draped magnetic fields, and this was later confirmed with multi-spacecraft data (Lai et al., 2015; 2019). Such field draping is assumed as the consequence of the solar wind interacting with clouds of charged dust particles released during interplanetary collisions, consistent with the stability of plasma parameters during an IFE. As evidenced by findings from the AMPTE (Ampère, Maximum Mission, Thermosphere, and Ionosphere) experiments (Valenzuela et al., 1986), the velocity differential between charged particles and the solar wind flow may deviate from the solar wind's primary direction, consistent with the observed normal to the interface. Further support comes from observations that sources of dust are common within the inner heliosphere, particularly along the orbits of asteroids and comets (e.g., He et al., 2019).

Recently, Fargette et al. (2021) reported similar phenomena observed by Parker Solar Probe (PSP) and referred to these events as "Magnetic Increases with Central Current Sheet" (MICCS), underscoring the central current sheet and aiming to avoid confusion with single flux ropes or other mesoscale forms of field compression in the solar wind. They further compared such solar wind structures on a scale of 0.3 million kilometers with the million meter (Mm)-scale flux rope interaction signatures observed in the magnetosheath (Oieroset et al., 2016; Zhou et al., 2018; Qi et al., 2020). They proposed that these solar wind structures are manifestations of interlaced magnetic flux ropes (IFRs), where the central current sheet occurs between colliding MFRs. This hypothesis is supported by the prevalence of MFRs at similar scales in the inner heliosphere (Crooker et al., 2006; Borovsky 2008; Zhao et al., 2021).

Both hypotheses can qualitatively explain some properties of IFEs, so neither can be ruled out yet. In the meantime, there is growing interest in these complex structures in the solar wind, targeted by recent missions including the Polarimeter to UNify the Corona and Heliosphere (PUNCH, DeForest et al., 2022). In addition, near-sun measurements from the PSP and Solar Orbiter (SolO) have shown the existence of such structures in high time resolution, warranting a comprehensive investigation to further examine these two interpretations.

In this paper, we employ sophisticated numerical models to systematically evaluate these two main hypotheses for the origin of IFE/MICCS: the dust model and the IFR model. We also refine and validate our numerical models using an event identified in STEREO data, thus contributing to a deeper understanding of these enigmatic mesoscale solar wind structures and

their impact on the solar system's dynamic environment.

2. Data and Model description

2.1 An event recorded by STEREO

In Figure 1, we present an example of an IFE/MICCS event, which was observed at 1AU by the STEREO-A (STA) spacecraft on October 20, 2008. The magnetic field measurements (STA_L1_MAG_RTN) were obtained using the magnetometer instrument from the In-situ Measurements of Particles And CME Transients (IMPACT) suite on STA (Acuña et al. 2008). Additionally, particle data associated with this event was collected by the Plasma and Suprathermal Ion Composition (PLASTIC) instrument (Galvin et al. 2008). The pressure shown in the bottom panel of Figure 1 is calculated from the plasma and field parameters.

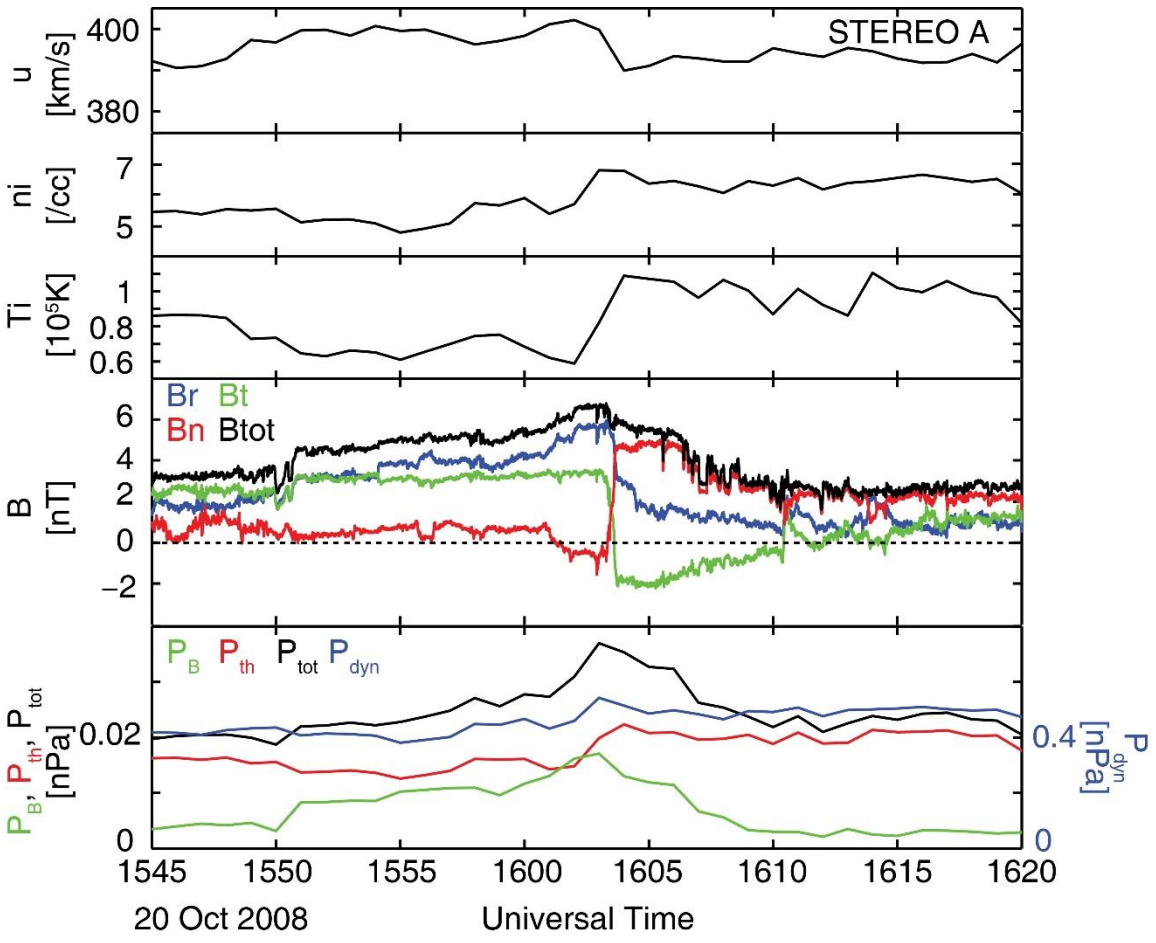

Figure 1. Top three panels: Plasma measurements from PLASTIC level 2 data at 1-minute resolution. The fourth panel: Magnetic field components at 1-second resolution in the RTN coordinate. Bottom panel: Calculated plasma thermal pressure P_{th}, magnetic pressure P_B, $P_{tot}=P_{th}+P_B$. The dynamic pressure P_{dyn} is labeled on the right.

The data are also plotted in a longer interval in supporting material Figure S1, where the suprathermal electron pitch angle data are also shown. No structures are seen in the magnetic field data next to this event, but there are density and temperature perturbations. Similar to some MICCS cases, no change in the electron pitch angle is discernible at the interface.

From this sample event, in about half an hour, the magnetic field strength B experienced a gradual increase of about 100%, followed by a gradual decrease back to the ambient value. Near the peak of this magnetic field enhancement, a distinct interface was identified where all three components of the magnetic field exhibited significant jumps, indicative of the presence of a thin current sheet.

In the trailing part of this interval, the ion density (n_i) showed a 20% increase, while ion temperature (T_i) displayed fluctuations with a 20% amplitude. The solar wind speed (u) exhibited a variation of barely 0.25%, with the most pronounced gradient occurring at the peak of the magnetic field enhancement. Notably, the change in *u* showed an inverse correlation with both *n* and *T*, albeit with a considerably smaller percentage.

The magnetic pressure (P_B) is lower than the thermal pressure of the plasma (P_{Th}), corresponding to a high beta plasma, and contributed most of the enhancement in P_{tot} ($P_{tot} = P_B + P_{Th}$). Intriguingly, the dynamic pressure ($P_{dyn} = n\times m\times u^2 /2$) also increased by about 20%, due to the density enhancement. Such an enhancement in both P_{tot} and P_{dyn} implies an energy transfer into this local interaction system of ions and the IMF. This observation aligns with the supposed energy input, which could either stem from a dust cloud, as suggested in a dust model (Lai et al., 2013), or from the entanglement process that concentrates plasma dynamic energy around the interface, as proposed in an IFR model.

The B magnitude observed in this event exhibits qualitative similarities with previously documented events of all different scales, as elucidated in the works of Russell et al. (1983), Lai et al. (2015), and Fargette et al. (2021). However, it is important to note that the profiles of *n*, *u*, *T*, and particle data in this event are individual rather than statistical. Generally, no generic or

typical plasma signatures have been reported for IFEs/MICCSs, and more investigation is needed. Consequently, the characterization and modeling of these parameters continue to be conducted on a case-by-case basis, and in our case with a focus on the magnetic field profiles. On the other hand, a dust model requires multiple fluids to handle the solar wind, dust cloud, and electrons, so a multi-fluid model is necessary. In contrast, the IFR model does not need to follow multiple fluids, but magnetic reconnection (MRC) may dominate during the process, so a Hall MHD model is used. These two different models and their results are detailed in the following sections respectively.

2.2 Dust model: Solar wind interaction with charged dust

In our dust model, we consider a scenario where a cloud of charged dust particles moves within the solar wind, as described in the initial conditions outlined in Figure 2. Any velocity disparity between the dust cloud and the surrounding solar wind plasma can lead to the bending and piling up of the IMF, potentially explaining the observed field enhancement. Lai et al., (2015) analyzed an IFE seen by five spacecraft and confirmed this draping signature. The thin current sheet near the magnetic field's peak is attributed to the IMF draping around the dust cloud (Russell et al., 1983).

Previous IFE investigations have identified several key constraints for these dust models: The speed of these structures closely matches the solar wind speed, so the relative speed between dust and solar wind is only a fraction of the solar wind speed and could point in any direction. To accelerate charged dust from its orbital speed to the solar wind speed within 1AU, the minimum distance from its origin must be approximately on the scale of its gyro-radius. If we assume a balanced surface potential of 10V in charging/discharging on such grains in the solar wind (Ragot and Kahler 2003), a maximum of seven positive charges per nm of radius of a dust particle can be carried. Instead of considering the upper limit of dust size, we opt for the smaller end, with dust particles having a radius of approximately 3 nm and a mass of 1×10^5 amu, carrying 21 charges. In a 0.3 AU solar wind with a 30-nanotesla (nT) magnetic field and a 0.5 Mm ion inertial length, the dust gyro-radius is about 700Mm or 0.004AU, and the gyro-period is about 3 hours. We note that such particles of nanometer size are smaller than the wavelength of visible and UV light, so they are invisible for direct optical observation. Instead, they may be detected by their physical or chemical interactions.

We employ a multi-fluid Magnetohydrodynamics (MHD) model based on the Michigan BATS-R-US code (Toth et al., 2012), as described by Jia et al. (2012). The model incorporates three fluid components: Dust, protons, and electrons, each calculated with their respective mass, momentum, and energy equations. The electron mass is assumed to be negligible. The simulation domain spans 40×20×20 Mm in a Cartesian grid, with the finest grid resolution set at 0.04 Mm around the dust cloud. The resolution of the coarsest grid at the boundaries is 0.16 Mm.

To cause a sufficiently large disturbance to the IMF, a cloud of dust particles is necessary. Given that the observed difference in number densities between solar wind electrons and protons is subtle during such events, we assume that the cloud is smaller than the observed structure. We impose the following initial condition for the dust, assuming no change exchange with the plasma, and let it move self-consistently as a fluid during the simulation. We employ a spherical Gaussian function centered at the origin (r=0) to determine the number density of dust in the cloud: $n_D = Q \times A^3 \times \exp(-(r/rH)^2/2)$, where coefficient $Q = 10^3$ /cc is the peak dust number density, $A = 1/(r_H \times \sqrt{2\pi})$ is the integration constant, and $r_H = 0.1$ Mm is the size of the dust cloud when density drops under Q/2. The dust temperature is assumed to be $T_D = 200$K, which is comparable to the surface temperatures of asteroids or comets.

Solar wind conditions from the event data are applied as initial conditions in the entire domain, and also inflow conditions at the upstream boundary (x=–10Mm): $n_{sw} = 5$/cc, $T_{sw} = 10^5$ K, IMF B = (2, 3, 0) nT, and plasma speed u defined below. All parameters are applied with 0-gradient outflow conditions at the rest five outer boundaries. As shown in the left panel of Figure 2, the x-coordinate in this local interaction system is aligned with the relative speed u (red arrows) between the solar wind and dust, while the arbitrary y and z complete the right-handed orthogonal system but are not yet associated with any vectors in the Radial-Tangential-Normal (RTN) coordinate. Consequently, the alignment of the spacecraft's trajectory remains undetermined in our simulation coordinate. We presume this relative speed to be roughly 15% of the solar wind speed, u = 60 km/s.

The right panel of Figure 2 shows an electron number density (n_e) contour in the sliced plane y=z. Because of the dust cloud obstacle, the solar wind plasma diverts in both the x and z-direction to generate an asymmetric wake (Jia et al., 2012) or the “anti-Hall effect” (Kriegel et al., 2014), so both magnetic and plasma perturbation profiles along different line cuts are expected to differ significantly in both intensity and shape. Shown by the B vectors and n_e

contours, such perturbations are evident within 10 Mm around the dust and extend about 20Mm downstream. Meanwhile, the shape of the dust cloud did not change significantly. All these disturbances remain stable over tens of minutes, with gradual expansion downstream of the interaction region. We note that this time scale monotonically increases with the space scale of the dust cloud in our other test runs within this mesoscale: Such structures last hours around a 10Mm scale dust cloud (not shown).

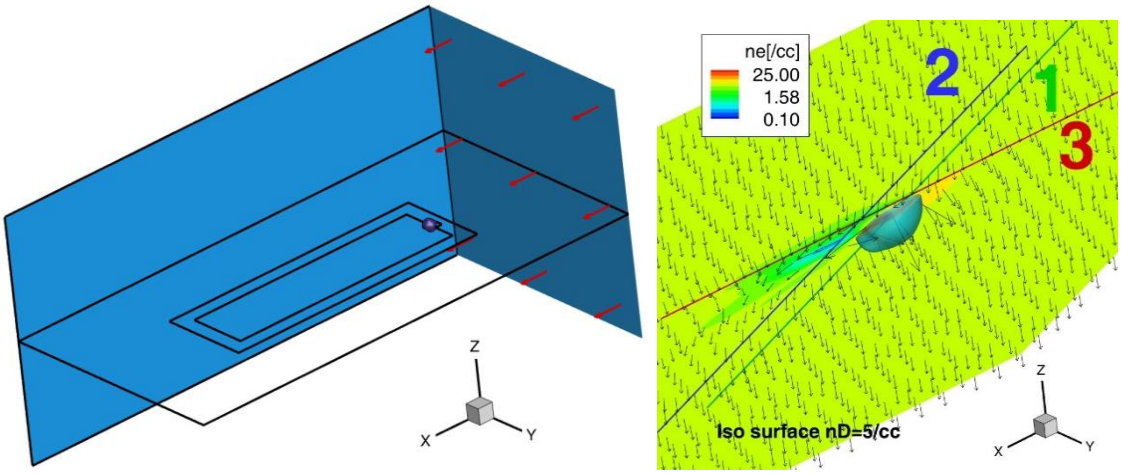

Figure 2. The 3-D plots of dust model result. The left panel shows the initial state with black rectangles marking the boundary of the grid resolution change. The dust cloud is represented by the purple sphere at the origin. The red arrows mark the direction of the inflowing solar wind. The right panel shows interaction around the dust at 8 minutes in a magnified view. The black arrows mark the 3-d magnetic field directions, and their lengths are proportional to their respective magnitudes. Color contour is the electron density sliced in the y=z plane. The three colored lines with labels are representative virtual paths where modeled values are extracted.

Based on the perturbations indicated by the density contour and field arrows, we picked three representative trajectories (labeled 1, 2, and 3 in Figures 2 and 3) to extract the modeled results and compare them with the observation. The interaction result presented in Figure 3 is extracted along the three colored lines at T=8 minutes in the right panels of Figure 2. The green line, characterized by the equation x=0, y=z, goes through the dust cloud. The blue line,

described by x=1, y=z, probes across the tail. The red line runs parallel to the flow in the local interaction frame and satisfies y=z=0.5 Mm.

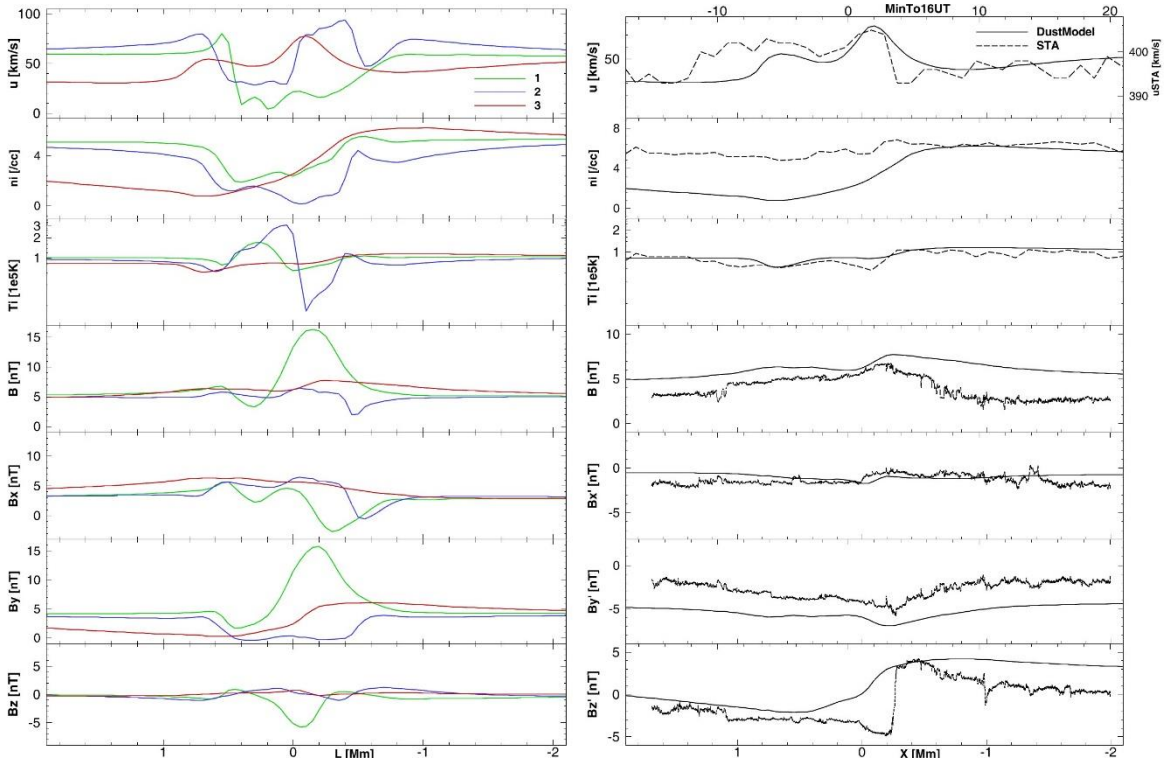

Figure 3. The left panels show the modeled result along the three lines of the same color and label shown in Figure 2. The red lines are arranged by the x-coordinate, while the rest go by y, as labeled at the bottom. The right panels compare STA event data with our modeled values extracted along the red line. All STA data are shown as dashed lines arranged by the same minutes from 16:00UT as labeled on top. All model results are in solid lines arranged by their same x-coordinate, as labeled by L at the bottom. The proton velocity is plotted at different scales: Our dust model result is labeled on the left, and STA measurement is labeled on the right. The magnetic field components (Bx', By', Bz') are in MVA coordinates.

The asymmetry in field enhancement along the green line that goes through the dust cloud is a result of this 3-D interaction, where the convection electric field (in the z-direction) persists because of the immobility of the massive dust cloud, pushing the tail in both x and z direction. Consequently, the magnetic field piles up on both the $x<0$ and the $y=z<0$ side. In

addition, the upstream side is the x<0 side, while the downstream side is the direction where all x, y, and z >0.

Because the dust is sparse and positively charged, the compression in ion density around y= – 0.6 Mm is small, and drops behind this pile-up region, while the ion speed slows down. The ion temperature does not change much on the upstream but enhances after the peak of magnetic field pileup at y=0 Mm, possibly raised where the refilling flows collide from multiple directions in the wake. The magnetic field magnitude B enhances as it piles up around y=0, and then decreases in the wake after y > 0.2 Mm. The 200% enhancement in the magnetic field is stronger than the strongest enhancement in previous IFE data (163% by Russell et al., 1985), but we note that the likelihood of detecting these extreme perturbations in solar wind data remains small, due to the relatively small size of the dust cloud (0.3Mm at T=8 min) when compared to the overall scale of the entire perturbed region (over 3Mm along the red line).

Along the blue line that is parallel to the green line in space but shifted along x, the effect of rarefaction can be seen from all parameters. The plasma density and temperature show stronger disturbance than these along the green line, because this blue line probes deeper in the wake, while the green line is at the beginning of the wake. The perturbation to the magnetic field is smaller along the blue line than along the green line, also because the green line experiences the field pile up on the upstream side while this blue line is in the wake where the field decreases. Such a decrease in B magnitude may be a typical criterion while seeking support for the dust models in the solar wind data.

The signatures of the modeled perturbations are different along these three passes and have many fine structures. This complicates the direct comparison between observation and simulation results. On the one hand, we could look for more typical structures in the solar wind data; on the other hand, we can adjust the virtual spacecraft trajectory to find signatures with the most similarity, as represented by the red lines in Figures 2 and 3.

Along the red line, a field enhancement and a current sheet are seen at x=0 Mm, so we compare this type of signatures with the STA data, as plotted in the right panels of Figure 3. From –2 to 2 Mm along the x-coordinate, similar acceleration to the ions is seen between the model and STA data, associated with a decrease in density and temperature. In this dust model, this acceleration to the ion flow is caused by the dust moving in the y-z direction, as illustrated in Figure 1 by Jia et al., (2012). This region with ion density rarefaction extends beyond x=2 Mm

down the wake. Also in this region, the magnetic field piles up and drops back across this shown distance of 4 Mm, similar to the STA data. This field pile-up is because of the averaged electron velocity is also diverted in the y-z direction in this region. Similarly, the pressures of the model result are compared with the data in the left panels of Figure S2. Because of the high-β nature of this solar wind, the total pressure is shaped similarly to the magnetic pressure, regardless of the density decrease. Such a combination of field enhancement with ion density decrease is often seen in dust-plasma interaction models because of the difference between bulk velocities of ions and electrons, but not obvious in the data of this event.

Because of the uncertainty in the relative velocity vector of the solar wind in the dust frame, the components of the magnetic field cannot be compared directly. Instead, we rotate the model result and STA data into their minimum variance analysis (MVA) coordinates (Goldstein, 1983), respectively. The B components are shown in their minimum (x'), intermediate (y'), and maximum (z') variance coordinates. Rather than a tail current sheet, the jump in Bz' of the model result is at the interface around x = 0 Mm between ion density pile-up and expansion regions.

In general, we find qualitative agreement with the STA data, except the current sheet is less sharp in the model, indicating a denser dust cloud than the one we used. On the other hand, the difference between the perturbations along the three examined paths suggests that the interaction region is complex and may exhibit different types of signatures along alternate paths. In the right panels of Figure 3, the comparison is applied between observed data arranged by time, with modeled results arranged by spatial scale. The scale of the structure in the STA data can be estimated by the product of the solar wind speed and the period, which is considerably greater than the scale in our model. Consequently, we can only confirm that the shapes are similar, rather than their sizes being quantitatively the same. Nonetheless, the qualitative consistency between the dust model and STA data motivates us to develop the next stage of such dust models. By adjusting a wide range of parameters discussed above, we support the use of such dust models to quantitatively reproduce the event data.

2.3 Interlaced flux-rope model

Numerical study of IFRs has been practiced in the solar corona (e.g., Linton et al., 2001) and the terrestrial magnetosheath (e.g., Jia et al., 2021). These models involve the interaction of

two MFRs, with a non-zero impact angle between the axes of these MFRs. The compression of these two ropes into an interlaced configuration also requires the presence of plasma flow shear, and this compression, along with the field enhancement at the center of both MFRs, is associated with the observed field enhancement. At the interface of these interlaced MFRs, a current sheet forms, resembling the one observed in the context of IFE/MICCS events.

In this study, we employ the same Hall MHD version of the BATS-R-US code (Toth et al., 2008) that has been used to simulate MFR interactions in the magnetosheath (Jia et al., 2021). In this 3-D simulation, the initial plasma condition is given by n = 5/cc and $T_i = 2.5 \times 10^5$ K, both in the background and in the MFRs. The Cartesian simulation grid spans 4000 × 2000 × 2000 Mm, with the finest spatial resolution set at 16 Mm. Two plasma flows, each with a speed of u=±13 km/s, are driven against each other along the x-direction.

As depicted in the top left panel of Figure 4, the initial configuration of the MFRs is determined by the force-free cylindrical model (Lundquist, 1950):

$B_{r'}=0$, $B_{\varphi'} = HB_0J_1(\alpha r'/R_0)$, $B_{z'}= B_0J_0(\alpha r'/R_0)$ when $r' \leq R_0$

$B = 0$ when $r' > R_0$

Here, r', φ', and z' represent local poloidal coordinates. The rope axis z' is set parallel to the z-axis for the left MFR and to the y-axis for the right MFR, indicating a simplified impact angle of 90°. The axial field B_0 = ±13nT. The parameter H=±1 denotes the handedness or chirality of the helical magnetic vectors. Functions J_0 and J_1 are the 0th and 1st-order Bessel functions, respectively. Constant R_0 = 130Mm is the radius of the MFR, and the constant α = 2.405 defines the ratio between the azimuthal component and axial component (Imber et al., 2014).

The panels of Figure 4 portray the time evolution of these interlaced MFRs. After 7 hours, these MFRs are merging into each other, comparable to the middle stage categorized by (Qi et al., 2020). At T=10 hours, most of the reconnection is done, while some remaining fluxes are still interacting. The MFR from –y reconnects with the one ending at +z, while –z connects with +y after 17 hours (bottom right panel). Consequently, these newly formed ropes move freely with the plasma flow. We note that at this stage, the red line is no longer probing through these structures, a different virtual trajectory would be needed to see the two separating MFRs.

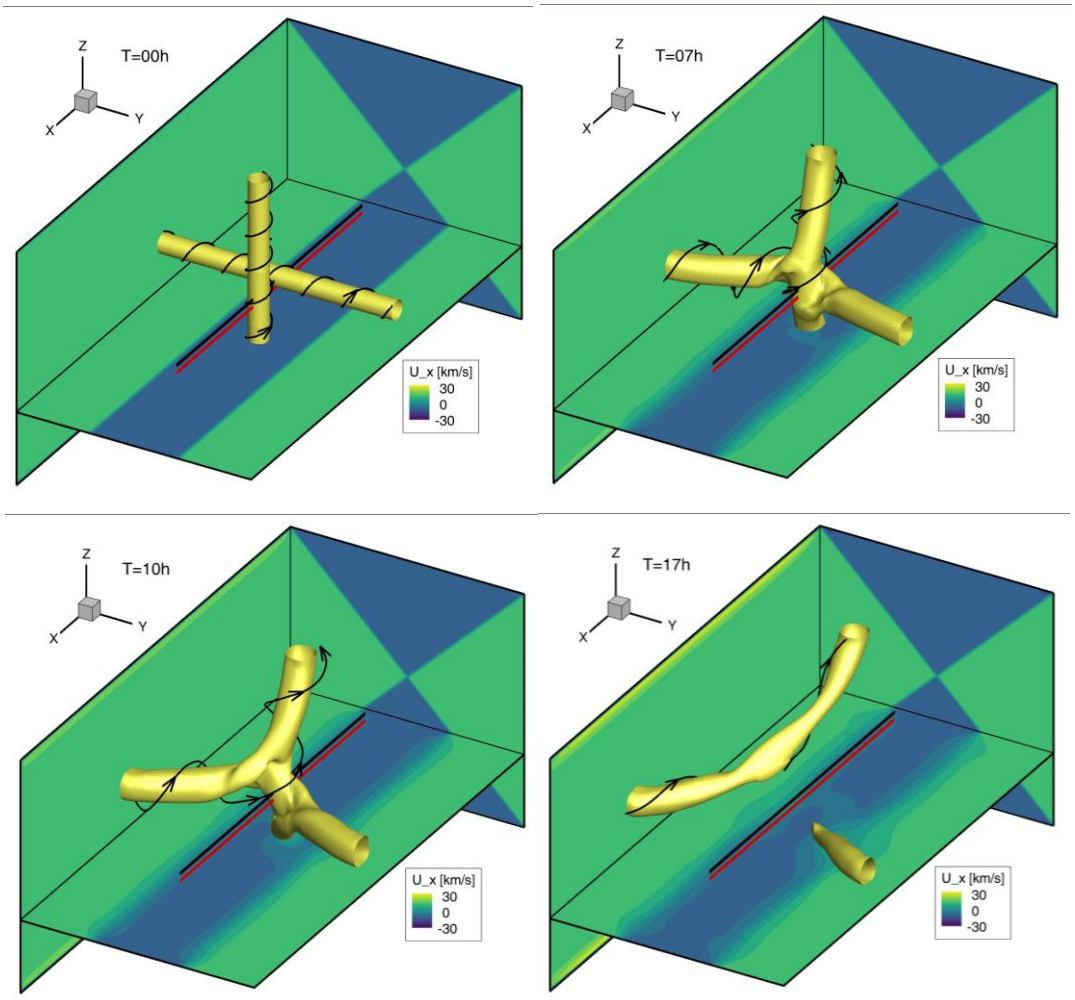

Figure 4. The top left panel shows the initial and boundary conditions of the IFR models. The black curves are field lines, winding around the yellow surfaces (iso-surface of magnetic field *B*) that represent the MFRs. The color contours at x= –2000, y= –1000, and z= –360 Mm show ion speed component u_x applied as fixed values. The black line in the center marks the x-axis, and the red line shows where model results are extracted. Other panels show the model results at T= 7, 10, and 17 hours.

Different from the dust model, we have found this MFR interaction symmetric, and thus the perturbation profiles along line cuts are similar. Along the red lines (y=0, z= –60) Mm in Figure 4, we extracted IFR model results to compare with the STA event, as plotted in Figure 5. The left panels of Figure 5 show the time evolution of parameters along the same line, but at 4, 7, and 10 hours during the modeled evolution. In the velocity panel, the original u_x shear evolves into a weaker flow between x=0 and 150 Mm. These persisting flow regions are caused by a u_y

component that is generated when the disconnected parts of the magnetic flux are moving to connect with the new ones. This speed is relatively small at T=4h while fully developed after T=7h.

Given that the entire domain starts with uniform density and temperature as its initial condition, variations in these parameters remain limited during the evolution. Specifically, the small bump in temperature represents heating at the interface of the interaction. Because of the z-offset of this line where we extract the modeled parameters, this interface retracts along –x over time. The shapes of magnetic field signatures are not significantly different, except the intensity becomes weaker over time. Similar interfaces can be seen in the u and B curves. The asymmetry in B is also caused by the z-offset of the path. At T=4h, most of the MFRs are kept intact, so the enhanced magnetic field is flat on top, rather than a typical cusp-shaped IFE/MICCS. Such a flat-top curve is comparable to events shown in panels 4,7,13,15, and 20 in Figure 5 of Fargette et al., (2021). These different types of perturbation call for observational support to validate this model.

The enhancement in B_x at T=4h represents the MFR on the –x side introduced by the initial condition. This trajectory goes through the center of the other MFR, on the +x side, so B_x remains 0 at +x. Similarly, the B_y and B_z components exhibit signatures from the two MFRs with a moving interface. This interface is comparable with the current sheet shown in 3-D under magnetosheath conditions (Figure 4 by Jia et al., 2021). Because of the symmetry of this interaction, results extracted along other lines exhibit comparable shapes.

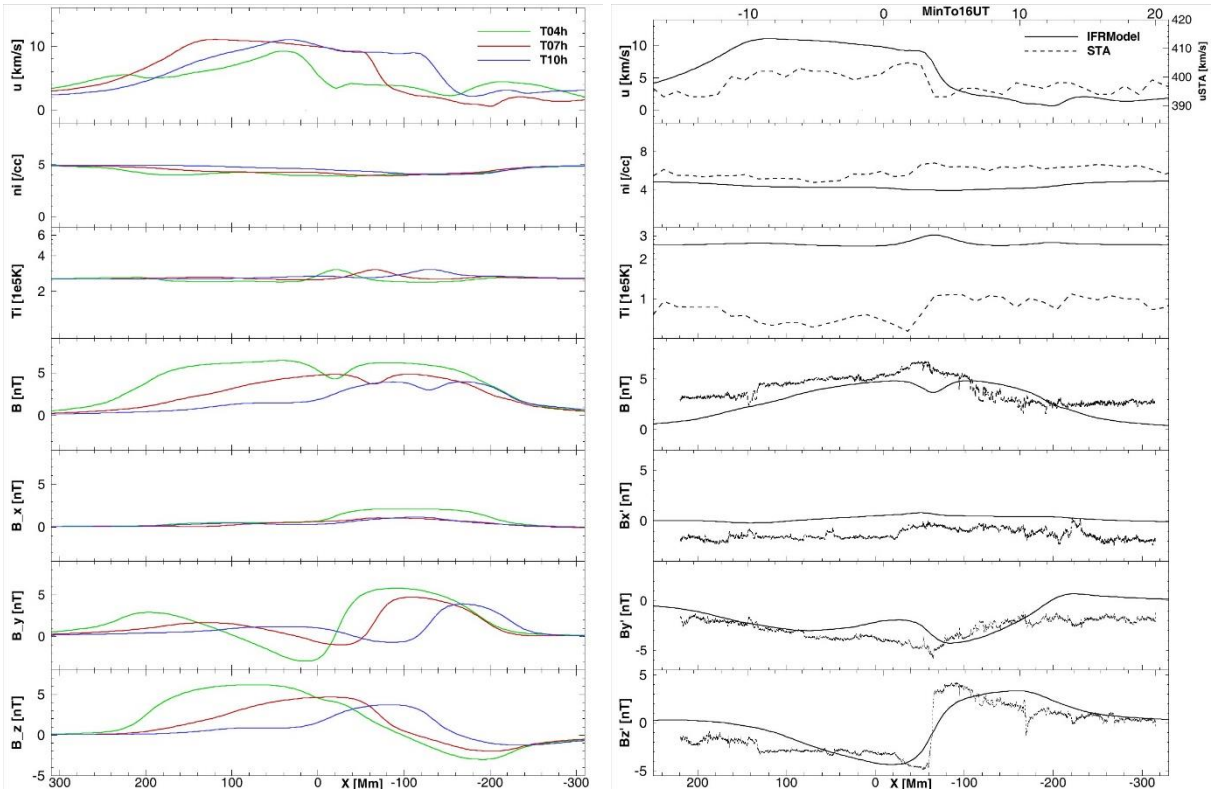

Figure 5. The left panels show modeled perturbation extracted along the same red line in Figure 4, but at different times of evolution: T=4 (green), 7 (red), and 10 (blue line) hours. The magnetic field components are shown in the simulation coordinate x-y-z. The right panel compares the IFR model results at T=7h with the STA measurement. Same as Figure 3, all STA data are arranged by the time in minutes from 16:00UT as labeled on top, while all model results are arranged by their x-coordinate labeled on the bottom. The proton velocity is plotted at different scales labeled on both sides. The magnetic field components are shown in their own MVA coordinate x'-y'-z'.

In the right panels of Figure 5, we plot the modeled parameters at T=7h against the STA observations, to compare the middle stage of the IFR profile with the data. Once again, the modeled results align closely with the observed data, reproducing the majority of the distinctive jumps. Although the speed profile matches the STA data relatively well, and a transverse velocity is also observed in the STA data, this u_y component is too small to affect the total solar wind speed in the data. In addition, the x-y-z components cannot be directly compared to the components in the STA data. A more detailed investigation is needed using both the velocity and

magnetic field components. The density perturbation seen in the STA data is not reproduced by our model. Whether this density difference in the data is caused by the density difference between the two types of plasma, or because of the interaction itself, calls for further investigation. The slight heating at the interface aligns with the data. In addition, as shown in the right panels of Figure S2, the pressure profiles are comparable, except for a decrease at the interface. The total pressures are shaped similarly, but the elevated temperature employed in this model also results in a higher total pressure profile.

Similar to what we did to the dust model, the magnetic field components are compared after rotating into their MVA coordinates. The modeled B magnitude also reproduced the notch in the center, which is caused by the current sheet as can be seen in the maximum variance component $B_{z'}$. Such a notch is obvious only in some IFE/MICCS events, e.g. Figures 3 and 5 by Fargette et al., (2021). For events where this notch is absent, it could be attributed to insufficient time resolution, or the trajectory missing the central current sheet. The $B_{y'}$ structure between x=0 and 50Mm matches the shape of the observed $B_{y'}$. The sharpness of the current sheet is not reproduced. As noted above, we expect a sharper interface and thinner notch with higher resolution models, or with kinetic models that can reproduce the current sheet better.

We extracted our model results along other lines: (y=0, z= +60), and (y=±60, z= 0). After the MVA rotation, the profiles are similar. Again, the magnetic field components in this IFR model result are not highly dependent on the trajectory.

3. Discussion and conclusions

In this study motivated by the desire to test two competing hypotheses concerning IFE origins, we have achieved qualitative reproduction of an observed event using both the dust model and the IFR model. While these models offer valuable insights and alignment with the observed data, certain disparities necessitate further investigations and model refinements to either invalidate one or the other or to perhaps support the validity of both.

We note that the model-data comparisons presented here are preliminary. As mentioned earlier, the results we have described are based on models using scales different from those of the observed structures, and different from each other. Given the observed similarity of these mesoscale structures ranging from minutes to hours, and the resemblance in our model results

444 across various scales within the self-similar fluid regime (not shown), our findings indicate that a
445 more thorough quantitative comparison at the same scales could yield deeper insights.
446 The dust model draws support from associations with potential dust sources (e.g., Russell
447 et al., 1984; Jones et al., 2003; He et al., 2019). Our model indicates that the dust cloud required
448 to generate such an enhancement could be over an order of magnitude smaller in scale, as
449 demonstrated in Section 2.2. This could explain why no in situ dust signals were observed during
450 PSP events (Fargette et al. 2021). According to our model calculations, when dust signals are
451 observed with sufficient density, the resulting plasma perturbations would likely surpass the
452 100% magnetic field increase observed in IFE/MICCS events.
453 One of the challenges of dust models lies in explaining the presence of thin current sheets
454 at the center of the disturbed IMF. In the STA data shown in Figure 1, the current sheet lasted
455 about 25 seconds. This converts to a 10Mm maximum thickness, which is several times the
456 1Mm-scale proton gyro radius. Such a kinetic-scale current sheet indicates a supersonic
457 interaction in a dust model, where the AMPTE experiments are comparable (Valenzuela et al.,
458 1986). Otherwise, a subsonic interaction would result in an expanding current region of Alfven
459 wings at the downstream side (e.g., Jia et al., 2010 and 2012), which will show up as a wide field
460 reversal region in the data. Moreover, for a stable supersonic interaction, the momentum loading
461 into the solar wind needs to be strong, because weak momentum loading cannot create tail
462 current sheets, as can be seen from the supersonic wake behind the Earth moon (e.g. Luhmann et.
463 al., 2004). These constraints help to shape the dust density distribution function in future models.
464 The mass-charge ratio of dust particles has a relatively minor impact on the results since
465 we primarily study the solar wind's response to the dust, rather than the dust particle acceleration
466 itself. However, the shape and size of the dust cloud can influence the shape and size of the
467 interaction region and deserve further exploration. The size used in our current model suggests a
468 smaller but more condensed dust cloud, which may create sharper boundaries but is less likely to
469 be detected directly by spacecraft. Additionally, the relative velocity vector between the dust
470 cloud and the solar wind, in the MVA frame of the IMF vector, is another set of parameters that
471 should be explored in future models.
472 In our current model, we assume that the dust cloud has already reached speeds roughly
473 equivalent to the solar wind speed. However, for a comprehensive understanding of dust
474 dynamics, it is imperative to delineate the source region and the evolutionary mechanisms

governing these dust clouds within the context of an inhomogeneous solar wind. Further research and observational work are crucial to exploring the processes of acceleration and transformation that propel these dust clouds from their initial orbital velocities to attain the speeds characteristic of the solar wind.

In the IFR model, our plasma temperature is set higher than observed. This is necessary for the flux ropes to reconnect. Our tests show that without changing other parameters, the minimum temperature for the IFR reconnection to happen is 2×10^5 K. The effect of temperature in such IFR models has also been discussed by Jia et al., (2021) in the magnetosheath condition. Cases without full reformation of the MFRs may also be studied in future models, in search of improvement to the reproduction of the event data.

As Fargette et al. (2021) have pointed out, the MICCS events appear qualitatively similar to the entanglement events in the magnetosheath (e.g. Qi et al., 2020), both by the enhancement profile and the reconnecting thin current sheet. We are currently using a middle-late stage of an IFR reconnection process to successfully reproduce the STA event, so continuous MRC is assumed. We expect future IFR models to adopt higher resolution and kinetic effects that can address more accurate MRCs at the central current sheet to reproduce both MICCS and entangled flux ropes.

Another significant assumption of the IFR model is the presence of multiple ropes. Each of the ropes may contain plasma of different density, temperature, or particle pitch angle distribution, exhibiting different properties in the data. Such asymmetric MFR interactions, as well as all types of impact angle interactions, are also necessary to investigate.

Due to the change in the solar wind and IMF in the inner heliosphere, both models predict different observations at different locations. In contrast to the dust model, the IFR model does not require an acceleration stage. However, the stages before and after the MFRs collide, the impact angle of these MFRs, their distribution with the heliocentric distance, latitude, and solar activity, as well as their correlation to the statistics of MFRs, also need further investigation to build a complete picture of such interactions.

As can be seen in Figure S1, the STA event we selected here is in a relatively calm solar wind. We note that the plasma signatures in this event are not typical. As an example, Fargette et al. (2021) have found nine MICCS events with plasma data of sufficient resolution to discern pitch angle variations. Among these nine events, five displayed notable pitch angle dissipation

jumps at the interface. As reviewed by Jian et al., (2018), more IFE/MICCS events have been documented in recent years. Thus, more event studies using all types of high-resolution plasma signatures, including particle pitch angle distribution, plasma heating process, waves, and ion/electron jets are feasible and necessary for more constraint on both models. In addition, statistic studies are also needed to further classify IFE/MICCS events, to determine whether they are linked to dust-related phenomena instead of the IFR model.

In summary, we have demonstrated the challenges associated with testing two models of the IFE/MICCS phenomena. We thus advocate for comprehensive high-resolution, multi-point observations, and MHD plus kinetic simulation efforts to achieve a holistic understanding of these structures. The present endeavor has resulted in recognizing the potential validity of both models, thus forthcoming observational and modeling research should be directed towards distinguishing events that are caused by these two different processes.

While infrequent in the solar wind, IFEs/MICCSs possess sufficient field magnitude to impact the state of the terrestrial magnetosphere and other celestial bodies (Lai et al., 2019). Either of the two potential explanations, whether involving dust or flux ropes, contribute to understanding the conditions prevailing in interplanetary space, and thus would also contribute to space weather studies.

Acknowledgment

The first author acknowledges ChatGPT 3.5 for rewording most of the sentences to improve the English in this paper. We acknowledge support from STEREO, NASA award number 80NSSC21K1512. We acknowledge support from NASA award 80NSSC21K1691.

Data Availability Statement

The STEREO-A magnetometer data and plasma data are available at https://stereo-dev.epss.ucla.edu/l2_data.

The BARS-R-US code used in the study is available for download as a component of the Space Weather Modeling Framework at the University of Michigan (http://clasp.engin.umich.edu/swmf).

The model results are available in zip compressed ASCII .dat files by Jia (2024) at: https://doi.org/doi:10.5061/dryad.m0cfxpp9v..

References

Acuña, M. H., Curtis, D., Scheifele, J. L., Russell, C. T., Schroeder, P., Szabo, A., & Luhmann, J. G. (2008). The STEREO/IMPACT magnetic field experiment. Space Science Reviews, 136(1–4), 203–226. https://doi.org/10.1007/s11214-007-9259-2.

Arghavani, M. R., Russell, C. T., Luhmann, J. G., & Elphic, R. C. (1985). Interplanetary magnetic field enhancements in the solar wind: Statistical properties at 1 AU. Icarus, 62, 230–243, https://doi.org/10.1016/0019-1035(85)90120-4

Borovsky, J. E. (2008). Flux Tube Texture of the Solar Wind: Strands of the Magnetic Carpet at 1 AU? Journal of Geophysical Research: Space Physics, 113. https://doi.org/10.1029/2007JA012684.

Burlaga, Leonard F. (1971), Nature and origin of directional discontinuities in the solar wind JGR 76(19), https://doi.org/10.1029/JA076i019p04360

Connors, M.; Russell, C. T.; Lai, H. R. (2016), The unusual asteroid 2201 Oljato: Origins and possible debris trail, Planetary and Space Science, 123, p. 16-24, DOI: 10.1016/j.pss.2015.11.017

Crooker, N. U., Burton, M. E., Phillips, J. L., Smith, E. J., & Balogh, A. (1996). Heliospheric plasma sheets as small-scale transients. Journal of Geophysical Research, 101(A2), 2467–2474, https://doi.org/10.1029/95JA03148

DeForest, C., et al. (2022). Polarimeter to UNify the Corona and Heliosphere (PUNCH): Science, Status, and Path to Flight. 2022 IEEE Aerospace Conference, Big Sky, MT, USA, pp. 1-11. https://doi.org/10.1109/AERO53065.2022.9843340.

Fargette, N., Lavraud, B., Rouillard, A., et al. (2021). Magnetic increases with central current sheets: observations with Parker Solar Probe. Astronomy & Astrophysics, 650(A11). https://doi.org/10.1051/0004-6361/202039191.

Galvin, A. B., Kistler, L. M., Popecki, M. A., et al. (2008). The Plasma and Suprathermal Ion Composition (PLASTIC) Investigation on the STEREO Observatories. https://doi.org/10.1007/s11214-007-9296-x.

564 Goldstein, H., (1983). On the field configuration in magnetic clouds, Solar Wind Five, NASA
565 Conf. Publ., 2280,731.

566 He, J., Cui, B., Yang, L., et al. (2021). The Encounter of the Parker Solar Probe and a Comet-like
567 Object Near the Sun: Model Predictions and Measurements. The Astrophysical Journal,
568 910(1), id.7. https://doi.org/10.3847/1538-4357/abdf4a.

569 Hu, Q., Zheng, J., Chen, Y., Roux, J., & Zhao, L. (2018). Automated Detection of Small-scale
570 Magnetic Flux Ropes in the Solar Wind: First Results from the Wind Spacecraft
571 Measurements. The Astrophysical Journal Supplement Series, 239(1).
572 https://doi.org/10.3847/1538-4365/aae57d.

573 Jia, Y. D., Russell, C. T., Khurana, K. K., Toth, G., Leisner, J. S., & Gombosi, T. I. (2010).
574 Interaction of Saturn's magnetosphere and its moons: 1. Interaction between corotating
575 plasma and standard obstacles. Journal of Geophysical Research, 115, A04214.
576 https://doi.org/10.1029/2009JA014630.

577 Jia, Y. D., Ma, Y. J., Russell, C. T., Lai, H. R., Toth, G., & Gombosi, T. I. (2012). Perpendicular
578 flow deviation in a magnetized counter-streaming plasma. Icarus, 218(2), 895–905.
579 https://doi.org/10.1016/j.icarus.2012.01.017.

580 Jia, Y.-D., Qi, Y., Lu, S., & Russell, C. T. (2021). Temporal evolution of flux rope/tube
581 entanglement in 3-D Hall MHD simulations. Journal of Geophysical Research: Space
582 Physics, 126, e2020JA028698. https://doi.org/10.1029/2020JA028698.

583 Jia, Ying-Dong (2024). Magnetic field enhancements in the interplanetary solar wind: Diverse
584 processes manifesting a uniform observation type? [Dataset]. Dryad.
585 https://doi.org/10.5061/dryad.m0cfxpp9v

586 Jian, L. K., C. T. Russell, J. G. Luhmann, and A. B. Galvin (2018), STEREO Observations of
587 Interplanetary Coronal Mass Ejections in 2007–2016, The Astrophysical Journal, 855(2), 114,
588 DOI 10.3847/1538-4357/aab189

589 Jones, G. H., Balogh, A., Russell, C. T., & Dougherty, M. K. (2003). Possible distortion of the
590 interplanetary magnetic field by the dust trail of comet 122P/De Vico. Astrophys. J., 597,
591 https://doi.org/10.1086/379750.

592 Kepko, L., Spence, H. E., & Singer, H. (2002). ULF waves in the solar wind as direct drivers of
593 magnetospheric pulsations. Geophys. Res. Lett., 29(8), 39,
594 https://doi.org/10.1029/2001GL014405

595 Kriegel, H., Simon, S., Meier, P., Motschmann, U., Saur, J., Wennmacher, A., Strobel, D. F., &
596 Dougherty, M. K. (2014). Ion densities and magnetic signatures of dust pickup at Enceladus.
597 Journal of Geophysical Research: Space Physics, 119, https://doi.org/10.1002/2013JA019440.

598 Lai, H. R., Wei, H. Y., & Russell, C. T. (2013). Solar wind plasma profiles during interplanetary
599 field enhancements (IFEs): Consistent with charged-dust pickup. AIP Conference
600 Proceedings, 1539, 402–405. https://doi.org/10.1063/1.4811070.

601 Lai, H. R. (2014), Interplanetary Field Enhancements: The Interaction between Solar Wind and
602 Interplanetary Dusty Plasma Released by Interplanetary Collisions, Thesis (Ph.D.)--UCLA,
603 AAT 3620701; ISBN: 9781303912917

604 Lai, H. R., Russell, C. T., Jia, Y. D., Wei, H. Y., & Angelopoulos, V. (2015). Momentum
605 transfer from solar wind to interplanetary field enhancements inferred from magnetic field
606 draping signatures. Geophysical Research Letters, 42, 1640–1645.
607 https://doi.org/10.1002/2015GL063302.

608 Lai, H. R., Russell, C. T., Wei, H. Y., Connors, M., & Delzanno, G. L. (2017). Possible
609 potentially threatening co-orbiting material of asteroid 2000EE104 identified through
610 interplanetary magnetic field disturbances. Meteoritics & Planetary Science, 52(6), 1125–
611 1132. https://doi.org/10.1111/maps.12854

612 Lai, H. R., Russell, C. T., Jia, Y. D., & Connors, M. (2019). Dust clouds penetrating the bow
613 shock. Geophysical Research Letters, 46. https://doi.org/10.1029/2019GL085818.

614 Linton, M. G., Dahlburg, R. B., & Antiochos, S. K. (2001). Reconnection of twisted flux tubes as
615 a function of contact angle. The Astrophysical Journal, 553(2), 905–921.
616 https://doi.org/10.1086/320974.

617 Liu, Y. Y., Fu, H. S., Cao, J. B., Yu, Y., Liu, C. M., Wang, Z., et al. (2022). Categorizing MHD
618 discontinuities in the inner heliosphere by utilizing the PSP mission. Journal of Geophysical
619 Research: Space Physics, 127, e2021JA029983. https://doi.org/10.1029/2021JA029983.

620 Luhmann, J. G., Ledvina, S. A., & Russell, C. T. (2004). Induced magnetospheres. Advances in
621 Space Research, 33. https://doi.org/10.1016/j.asr.2003.03.031.

622 Lundquist S (1950) Magneto-hydrodynamic fields. Ark Fys 2:361–365

623 Øieroset, M., Phan, T. D., Haggerty, C., Shay, M. A., Eastwood, J. P., Gershman, D. J., et al.
624 (2016). MMS observations of large guide field symmetric reconnection between colliding
625 reconnection jets at the center of a magnetic flux rope at the magnetopause. Geophysical
626 Research Letters, 43, 5536–5544. https://doi.org/10.1002/2016GL069166.

627 Qi, Y., Russell, C. T., Jia, Y. ‐ D., & Hubbert, M. (2020). Temporal evolution of flux tube
628 entanglement at the magnetopause as observed by the MMS satellites. Geophysical Research
629 Letters, 47, e2020GL090314. https://doi.org/10.1029/2020GL090314.

630 Ragot, B. R., & Kahler, S. W. (2003). Interactions of dust grains with coronal mass ejections and
631 solar cycle variations of the F-coronal brightness. Astrophys. J., 594, 1049–1059, DOI:
632 10.1086/377076

633 Russell, C. T., Luhmann, J. G., Barnes, A., Mihalov, J. D., & Elphic, R. C. (1983). An unusual
634 interplanetary event: Encounter with a comet? Nature, 305(5935).
635 https://doi.org/10.1038/305612a0

636 Russell, C. T., Aroian, R., Arghavani, M., & Nock, K. (1984). Interplanetary magnetic field
637 enhancements and their association with the asteroid 2201 Oljato. Science, 226(4670), 43–45.
638 https://doi.org/10.1126/science.226.4670.43

639 Russell, C. T., Schwingenschuh, K., Phillips, J. L., & Arghavani, M. R. (1985). Three spacecraft
640 measurements of an unusual disturbance in the solar wind: Further evidence for a cometary
641 encounter. Geophysical Research Letters, 12(7), 476–478.
642 https://doi.org/10.1029/GL012i007p00476.

643 Russell, C. T., J. L. Phillips, J. G. Luhmann, and J. A. Fedder, (1986). Interplanetary flux
644 enhancements: Comparison with cometary models and observations. Advances in Space
645 Research, 6(1), 191-194. https://doi.org/10.1016/0273-1177(86)90032-3

646 Russell, C. T., L. K. Jian, J. G. Luhmann, T. L. Zhang, F. M. Neubauer, R. M. Skoug, X. Blanco-
647 Cano, N. Omidi, and M. M. Cowee (2008). Mirror mode waves: Messengers from the coronal
648 heating region. Geophysical Research Letters, 35, L15101. doi:10.1029/2008GL034096.

649 Tóth, G., Ma, Y. J., & Gombosi, T. I. (2008). Hall magnetohydrodynamics on block-adaptive
650 grids. Journal of Computational Physics, 227(14), 6967–6984.
651 https://doi.org/10.1016/j.jcp.2008.04.010

652 Tóth, G., van der Holst, B., Sokolov, I. V., De Zeeuw, D. L., Gombosi, T. I., Fang, F., et al.
653 (2012). Adaptive numerical algorithms in space weather modeling. Journal of Computational
654 Physics, 231(3), 870–903. https://doi.org/10.1016/j.jcp.2011.02.006

655 Valenzuela, A., Haerendel, G., Foeppl, H., Melzner, F., Neuss, H. (1986). The AMPTE artificial
656 comet experiments. Nature, 320, 700–703. DOI: 10.1038/320700a0

657 Viall, N. M., C. E. DeForest, L. Kepko (2021). Mesoscale Structure in the Solar Wind. Front.
658 Astron. Space Sci., Sec. Space Physics 8. https://doi.org/10.3389/fspas.2021.735034

659 Zhao, L.-L., G. P. Zank, Q. Hu, et al. (2021). Detection of small magnetic flux ropes from the
660 third and fourth Parker Solar Probe encounters. Astronomy & Astrophysics, 650(A12).
661 https://doi.org/10.1051/0004-6361/202039298

662 Zhou, M., Berchem, J., Walker, R. J., El-Alaoui, M., Goldstein, M. L., Lapenta, G., et al. (2018).
663 Magnetospheric Multiscale observations of an ion diffusion region with large guide field at
664 the magnetopause: Current system, electron heating, and plasma waves. Journal of

Geophysical Research: Space Physics, 123, 1834–1852.
https://doi.org/10.1002/2017JA024517